Supplementary Information

Binding Azaphilic Copper Radioisotopes with All-Nitrogen Macrocycles for Cancer Theranostics

Sara Franchi [a], Mattia Asti [b], Nóra V. May [c], Silvia Pozzo [a], Sofia Gama [d], Erika Ferrari [e], Laura Pigani [e], Christian Jentschel [f], Christin Neuber [f], Fabrizio Mancin [a], Sven Stadlbauer [f], Klaus Kopka [f,g,h,i], Constantin Mamat [f], Helmut Mäcke [j], Valerio Di Marco [a], Marianna Tosato [k,l,*]

[a] Department of Chemical Sciences, University of Padova, 35131 Padova, Italy.
[b] Radiopharmaceutical Chemistry Laboratory, Nuclear Medicine Unit, AUSL-IRCCS Reggio Emilia, 42122 Reggio Emilia, Italy.
[c] Centre for Structural Sciences, HUN-REN Research Center for Natural Sciences, 1117 Budapest, Hungary.
[d] Center for Nuclear Sciences and Technologies, Instituto Superior Técnico, University of Lisbon, 2695-066 Bobadela, Portugal.
[e] Department of Chemical and Geological Sciences, University of Modena and Reggio Emilia, 41125 Modena, Italy.
[f] Institute of Radiopharmaceutical Cancer Research, Helmholtz-Zentrum Dresden-Rossendorf (HZDR), D-01328 Dresden, Germany.
[g] TUD Dresden University of Technology, School of Science, Faculty of Chemistry and Food Chemistry, D-01062 Dresden, Germany.
[h] German Cancer Consortium (DKTK), Partner Site Dresden, D-01307 Dresden, Germany.
[i] National Center for Tumor Diseases (NCT), NCT/UCC Dresden, D-01307 Dresden, Germany.
[j] Department of Nuclear Medicine, University Hospital Freiburg, D-79106 Freiburg, Germany.
[k] Department of Chemistry, Simon Fraser University, Burnaby, V5A 1S6, British Columbia, Canada.
[l] Life Sciences, TRIUMF, Vancouver, BC V6T 2A3, British Columbia, Canada.

*** Corresponding author**: marianna_tosato@sfu.ca

Supplementary Discussion

Formation Kinetics of Cu^{2+} Complexes with All-Nitrogen Macrocycles

The formation kinetics of Cu^{2+}-DO4N and Cu^{2+}-NO3N complexes were qualitatively explored by UV-Vis spectroscopy at room temperature (RT), several pH values (0, 1, 2, 3, 4, 7.4) and different reagent concentrations (10^{-4}, 10^{-3} M). These results yield preliminary data on the rate of metal complexation by the investigated chelators, a key consideration in radiopharmaceutical development, where rapid and efficient binding is required. Representative electronic spectra are reported in **Figures S19 - S21**, and the corresponding time-dependent absorbance changes are shown in **Figures S22 - S24**.

The rate of Cu^{2+}-DO4N formation is strongly pH-dependent: at $C_{Cu} = C_{DO4N} = 10^{-4}$ M, the equilibrium was reached almost instantaneously at pH ≥ 4, while at lower pH values the reaction slowed considerably, requiring ~ 15 min at pH 3 and a few hours at pH 2 (**Figure S22**). At pH 1, the equilibrium was attained only after heating at 65°C overnight, whereas no complex formation was observed at pH 0 even after prolonged heating (**Figure S22**), indicating that Cu^{2+}-DO4N formation is thermodynamically disfavored under highly acidic conditions (pH < 1), likely due to intense competition by protons. The observed kinetic behavior is consistent with the well-established observation that, as pH decreases, complex formation slows down since the ligand becomes progressively more protonated, both limiting the number of accessible donor sites and increasing electrostatic repulsion toward the incoming Cu^{2+} ion.[1-3]

The formation rate of Cu^{2+}-DO4N is also concentration-dependent, as expected: for example, increasing the concentration of Cu^{2+} and DO4N from 10^{-4} M to 10^{-3} M significantly accelerated the attainment of equilibrium, requiring only ~ 7 min at pH 3 and ~ 80 min at pH 2 (**Figure S23**).

The kinetics of Cu^{2+}-NO3N complex formation was investigated as well, as these data are not available in the literature to the best of our knowledge. The scenario was very similar to that of Cu^{2+}-DO4N: at $C_{Cu} = C_{NO3N} = 10^{-4}$ M, Cu^{2+}-NO3N complex formation was very rapid (< 2 min) at pH ≥ 4 but slowed dramatically at pH 2 (~ 20 h, **Figure S24**). At pH 1, the kinetics was sluggish, and equilibrium was attained only after overnight heating at 65°C (**Figure S24**). Only a small amount of Cu^{2+} complex formed at pH 1 (~ 29% compared to pH 2, by assuming the same molar absorptivity at 281 nm), in agreement with the low thermodynamic stability expected at this pH according to the study by Tei *et al.* (see main text).[4]

A comparison of the two systems reveals that Cu^{2+}-NO3N complexes form more slowly than those of DO4N, possibly due to higher energy barriers needed to attain the final geometry. The smaller ring size of NO3N might introduce greater steric hindrance and consequently reduce the rate of Cu^{2+} complexation.

Solid-State Structure of Cu^{2+}-DO4N

Due to ambiguities in atom assignment and uncertainties in locating hydrogen atoms, particularly at terminal nitrogen positions, the determination of the overall charge must be approached with caution. Based on the structural data, it is likely that three peripheral chloride ions are present, corresponding to the positive charges from Cu^{2+} and a doubly protonated H_2DO4N^{2+} ligand. Charge neutrality is therefore assumed to be achieved through the chloride ion coordinated axially to the Cu^{2+} center, and three acting as external counter ions positioned near side-chain amino groups. A further difficulty in this analysis was that the solvent molecules (water and ethanol) in the crystal cavities could not be localized and were therefore took into account using the Olex2 solvent mask option.

The packing arrangements along the three crystallographic directions are shown in **Figure S35**. The crystal structure displays large channels containing disordered ethanol and/or water solvent molecules (**Figure S36**).

Supplementary Figures

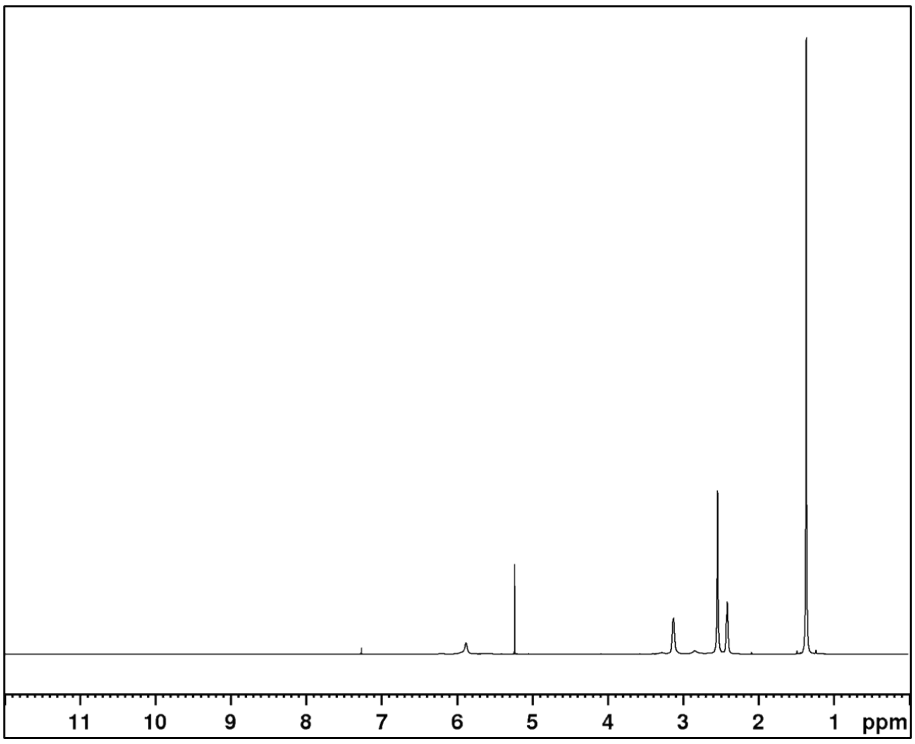

Figure S1. ^{1}H NMR spectrum of DO4N-Boc ($CDCl_3$, 500 MHz, T = 298 K). Signal at 5.24 ppm corresponds to traces of CH_2Cl_2.

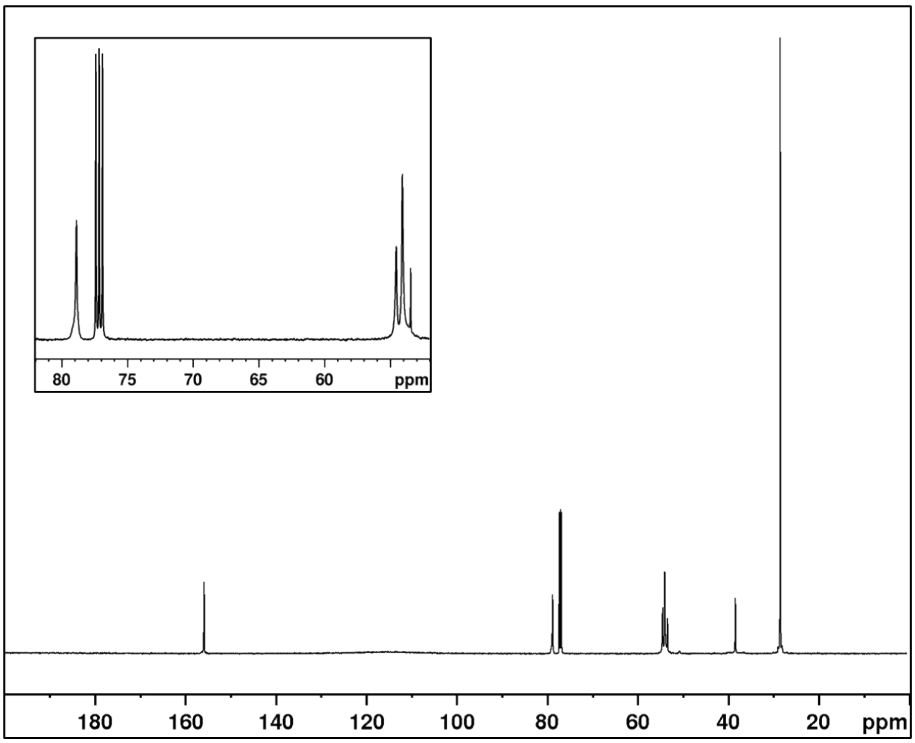

Figure S2. $^{13}C\{^{1}H\}$ NMR spectrum of DO4N-Boc ($CDCl_3$, 126 MHz, T = 298 K). Signal at 53.4 ppm corresponds to traces of CH_2Cl_2. The insert shows a zoom of the signals.

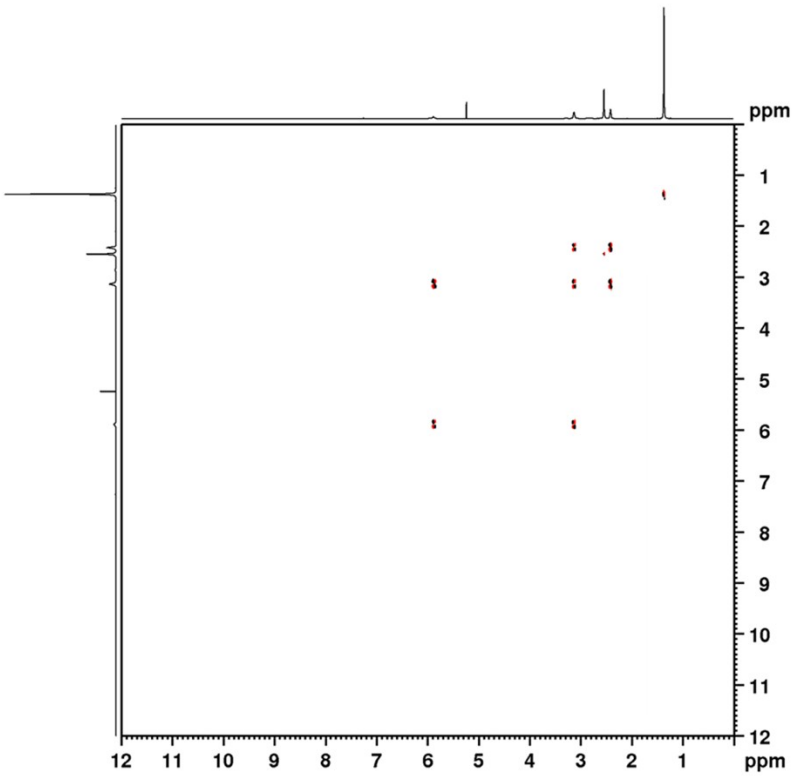

Figure S3. ^{1}H-^{1}H COSY spectrum of DO4N-Boc ($CDCl_3$, 500 MHz, T = 298 K). Signal at 5.24 ppm corresponds to traces of CH_2Cl_2.

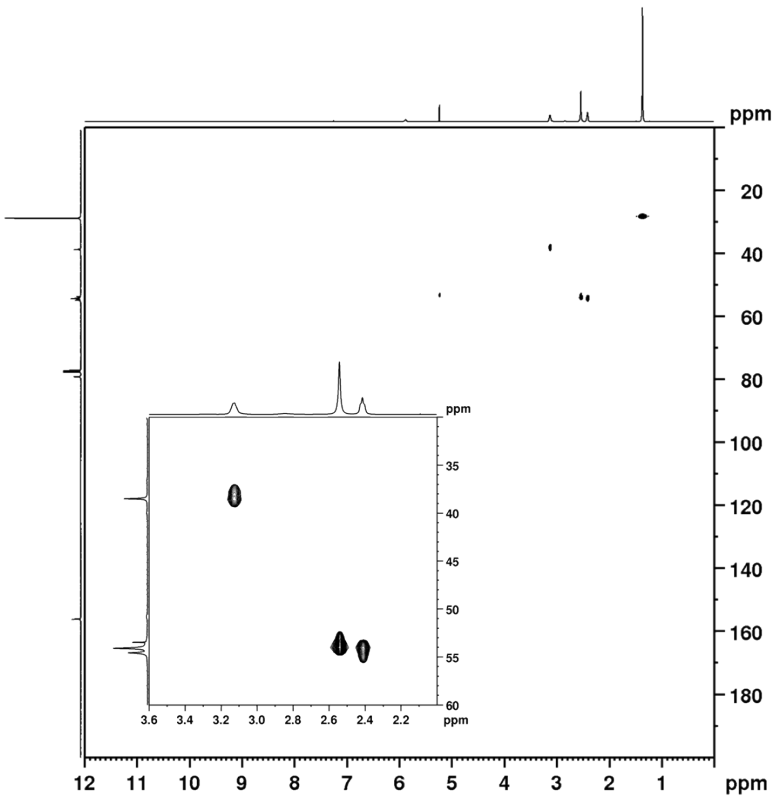

Figure S4. ^{1}H-^{13}C HSQC spectrum of DO4N-Boc ($CDCl_3$, 500 and 126 MHz, T = 298 K). Signals at 5.24 and 53.4 ppm correspond to traces of CH_2Cl_2. The insert shows a zoom of the signals.

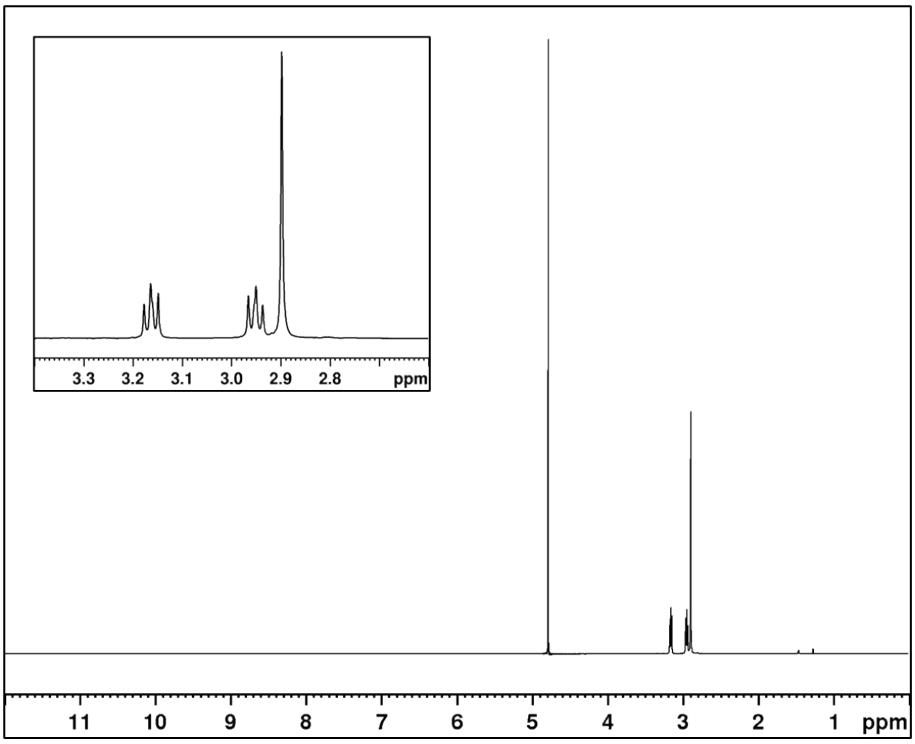

Figure S5. ^{1}H NMR spectrum of DO4N (D_2O, 500 MHz, *T* = 298 K, pH ~ 7). Signal at 4.79 ppm corresponds to residual proton solvent peak. The insert shows a zoom of the signals.

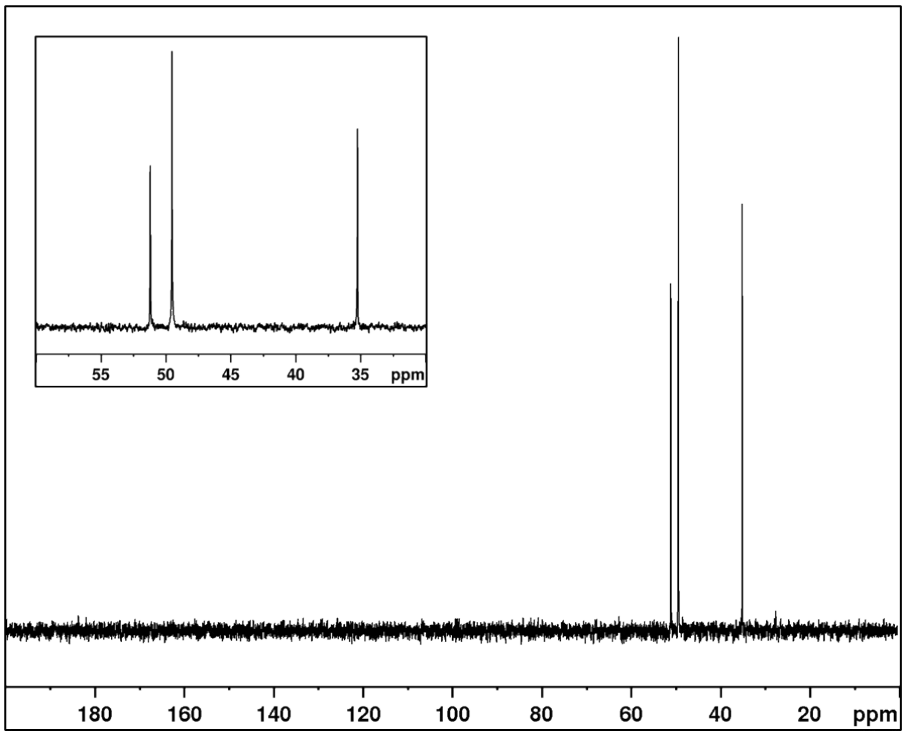

Figure S6. $^{13}C\{^{1}H\}$ NMR spectrum of DO4N (D_2O, 126 MHz, *T* = 298 K, pH ~ 7). The insert shows a zoom of the signals.

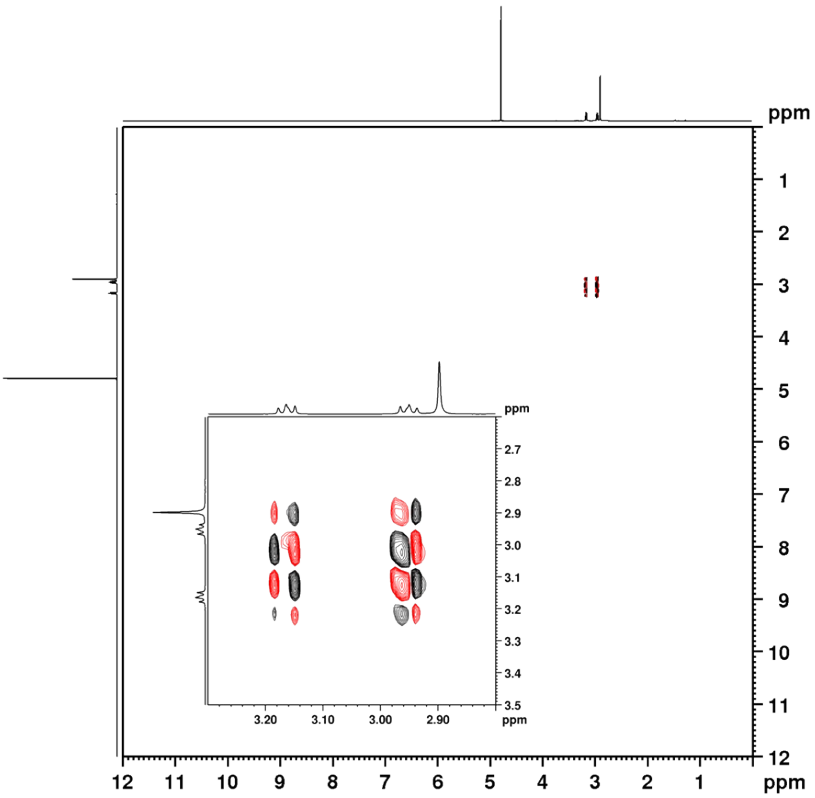

Figure S7. ^{1}H-^{1}H COSY spectrum of DO4N (D_2O, 500 MHz, *T* = 298 K, pH ~ 7). Signal at 4.79 ppm corresponds to residual proton solvent peak. The insert shows a zoom of the signals.

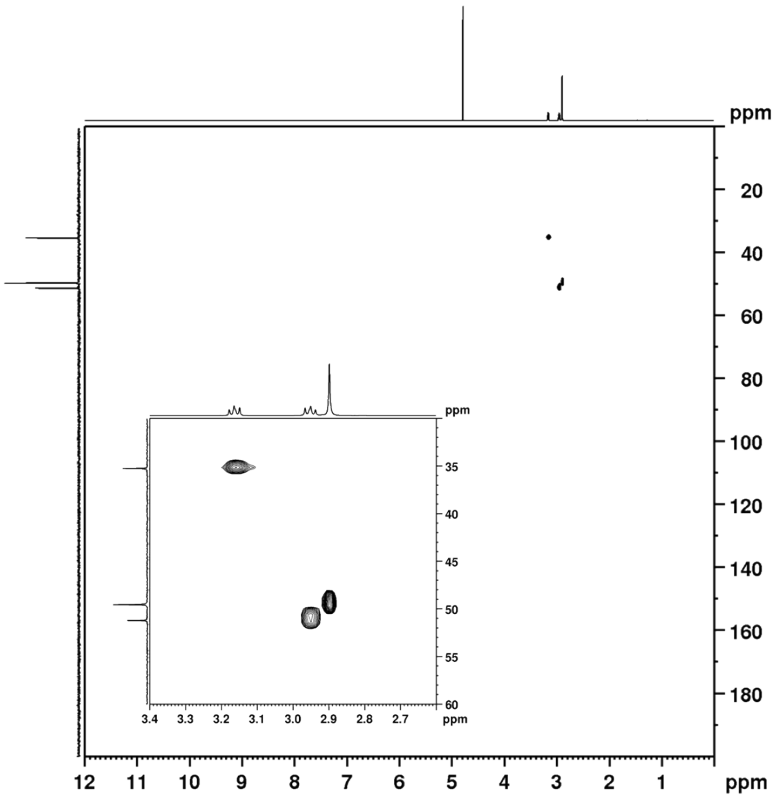

Figure S8. ^{1}H-^{13}C HSQC spectrum of DO4N (D_2O, 500 and 126 MHz, *T* = 298 K, pH ~ 7). Signal at 4.79 ppm corresponds to residual proton solvent peak. The insert shows a zoom of the signals.

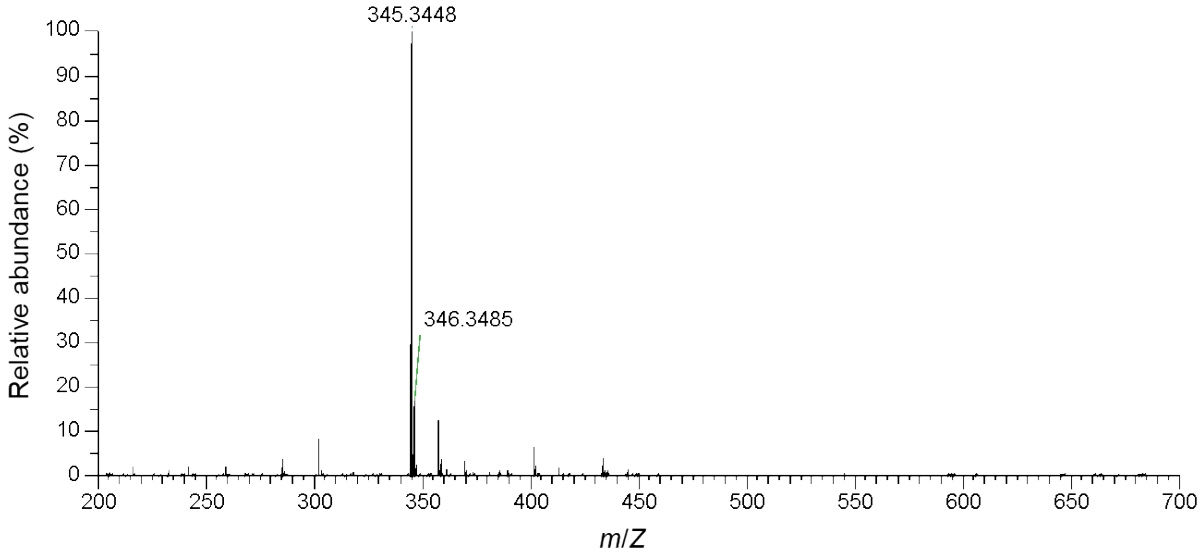

Figure S9. High-resolution mass spectrum of DO4N.

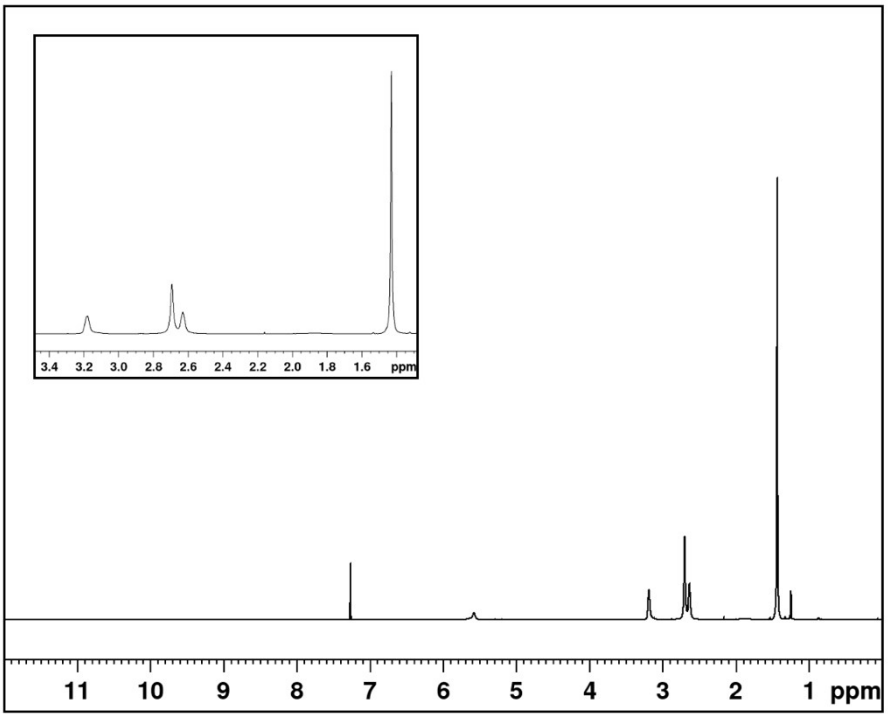

Figure S10. ^{1}H NMR spectrum of NO3N-Boc ($CDCl_3$, 600 MHz, *T* = 298 K). Signal at 7.26 ppm corresponds to residual proton solvent peak. The insert shows a zoom of the signals.

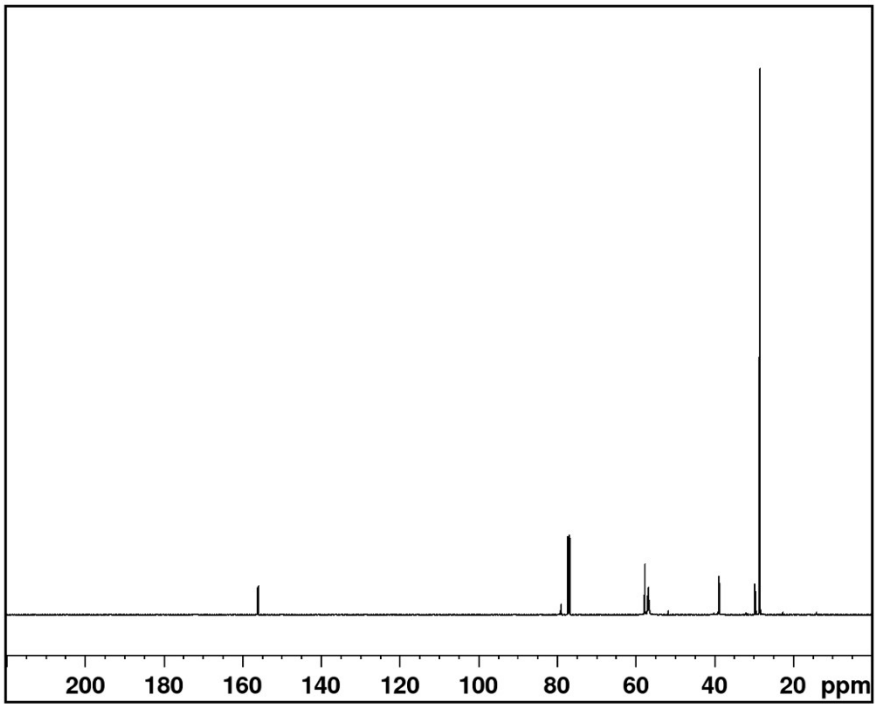

Figure S11. $^{13}C\{^{1}H\}$ NMR spectrum of NO3N-Boc ($CDCl_3$, 150 MHz, *T* = 298 K). Signal at 77.16 ppm corresponds to ^{13}C solvent peak.

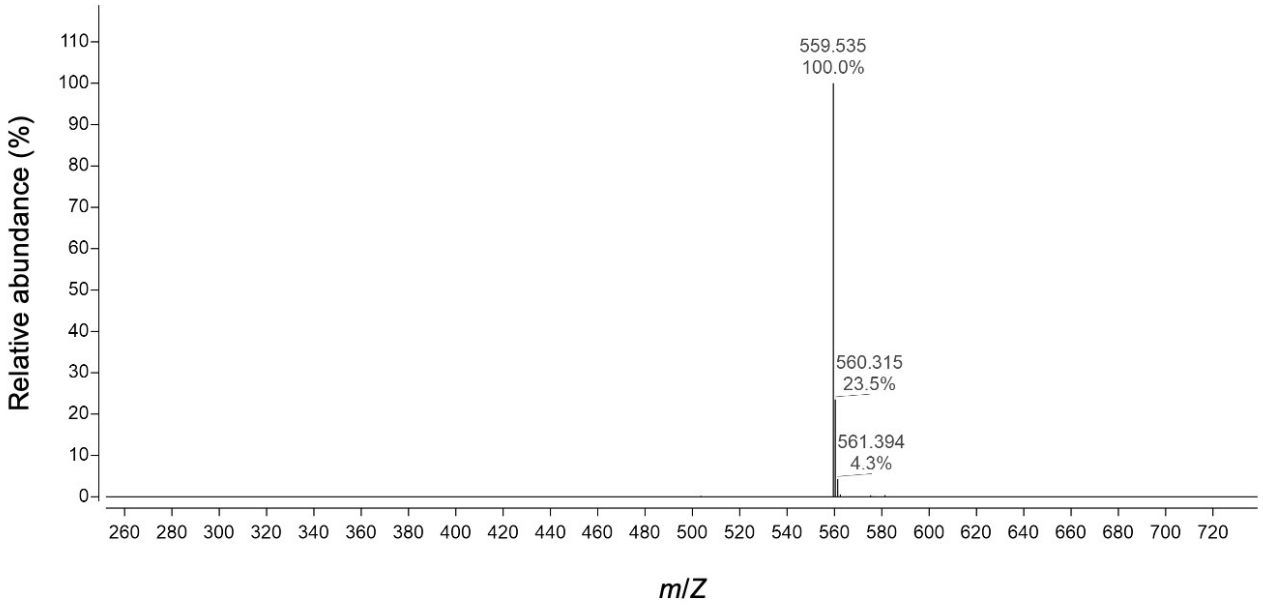

Figure S12. High-resolution mass spectrum of NO3N-Boc.

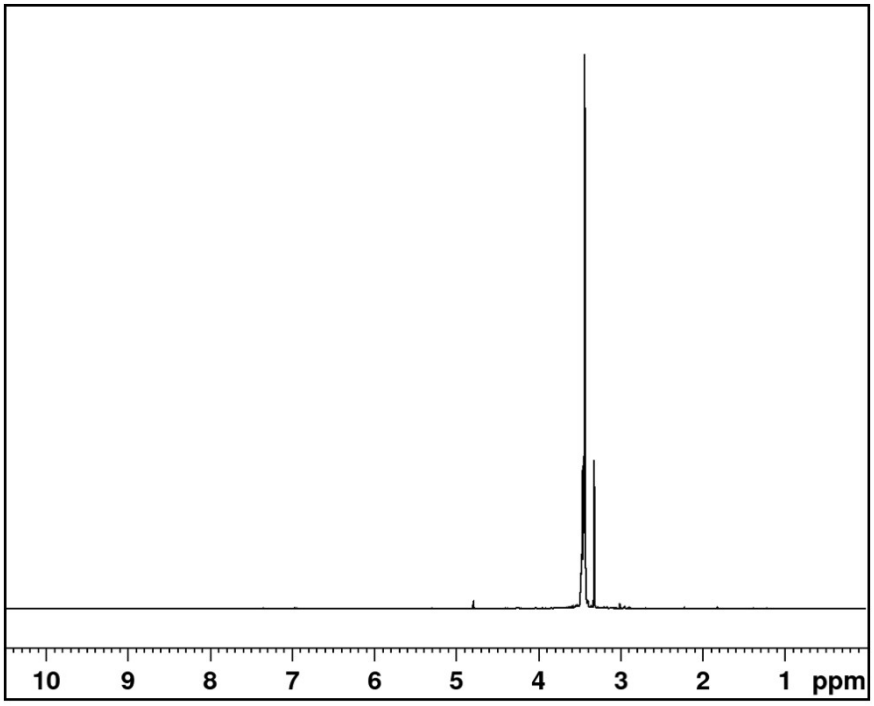

Figure S13. ^{1}H NMR spectrum of NO3N (D_2O, 600 MHz, *T* = 298 K). Signal at 4.79 ppm corresponds to residual proton solvent peak.

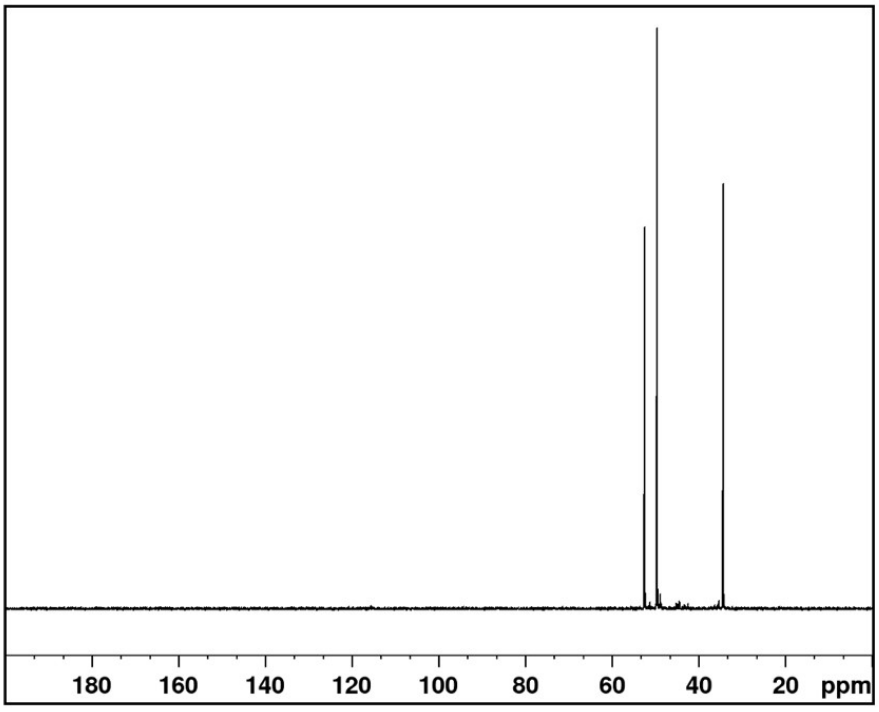

Figure S14. $^{13}C\{^{1}H\}$ NMR spectrum of NO3N (D_2O, 126 MHz, *T* = 298 K).

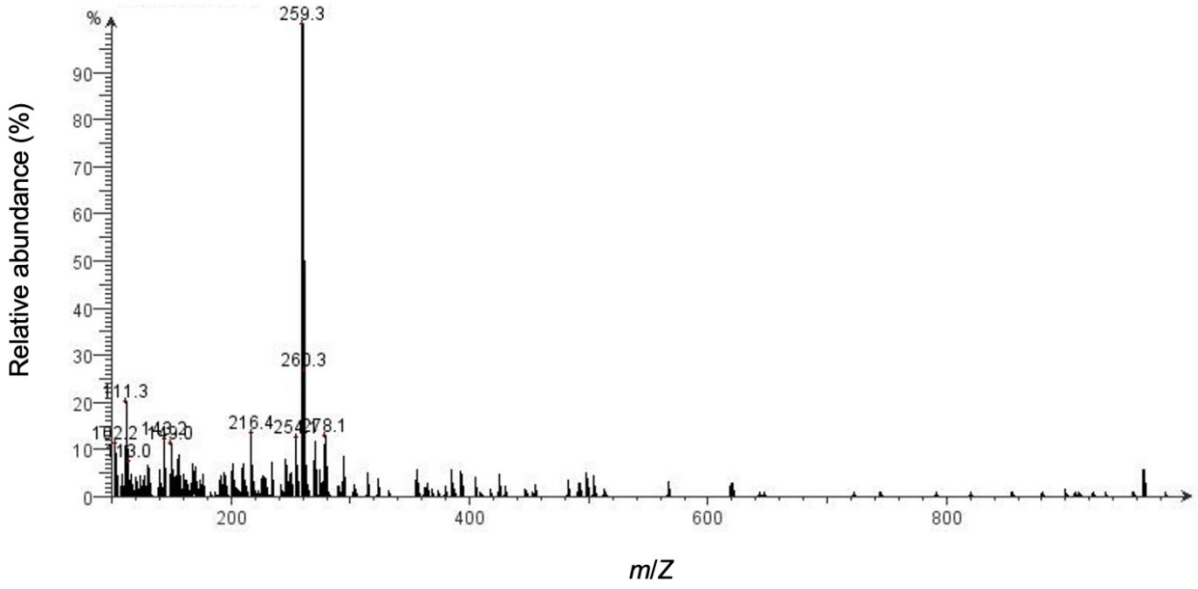

Figure S15. Mass spectrum of NO3N.

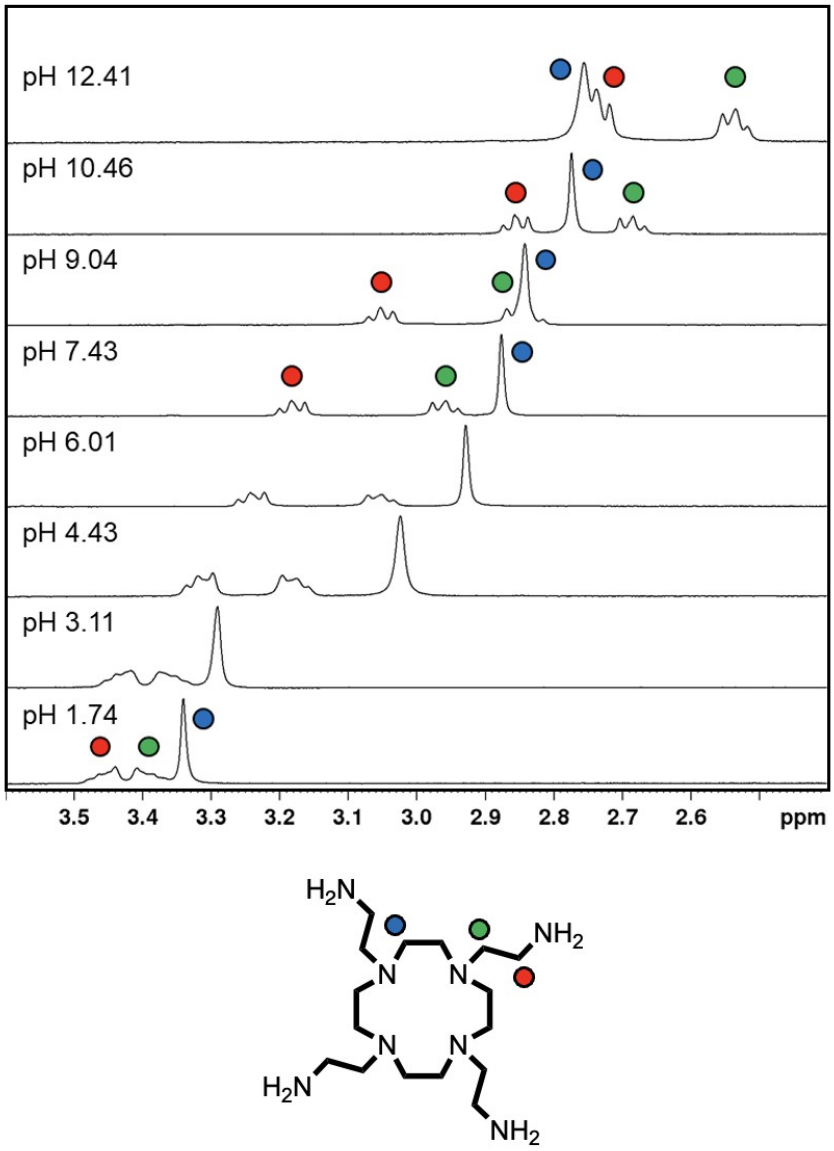

Figure S16. Representative pH-dependent ^{1}H NMR spectra of DO4N (90% H_2O + 10% D_2O, 400 MHz, T = 298 K, I = 0.15 M NaCl, C_{DO4N} = 10^{-3} M) and signal attribution.

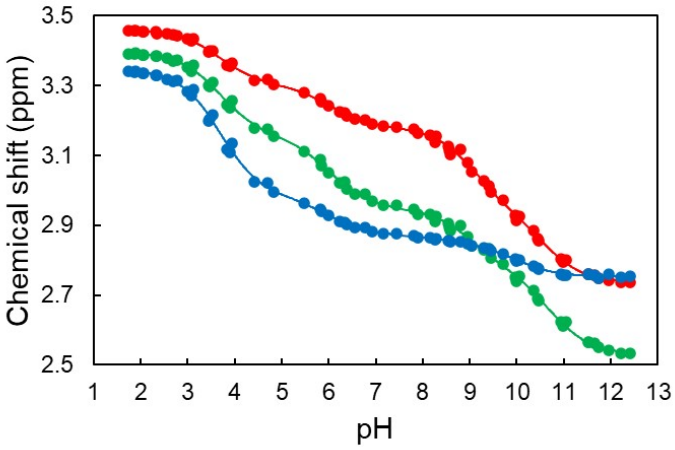

Figure S17. Chemical shift trend *vs* pH for each signal in the ^{1}H NMR titration of DO4N (90% H_2O + 10% D_2O, 400 MHz, T = 298 K, I = 0.15 M NaCl, C_{DO4N} = 10^{-3} M). See **Figure S16** for the color code.

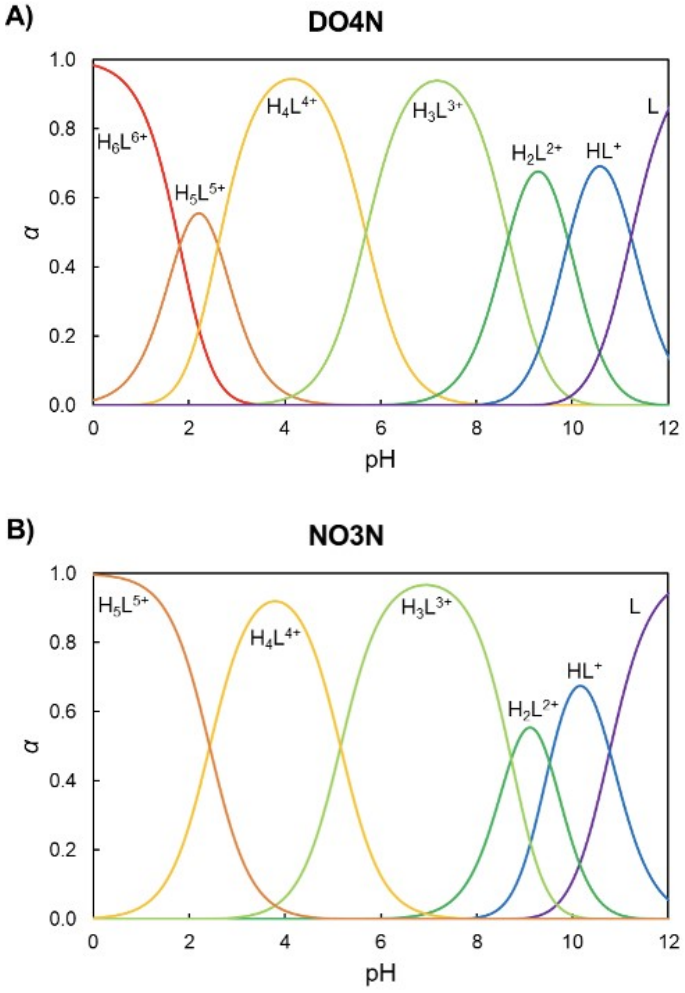

Figure S18. Distribution diagram of (A) DO4N and (B) NO3N. pK_a values were taken from either **Table 1** or ref. (4), respectively.

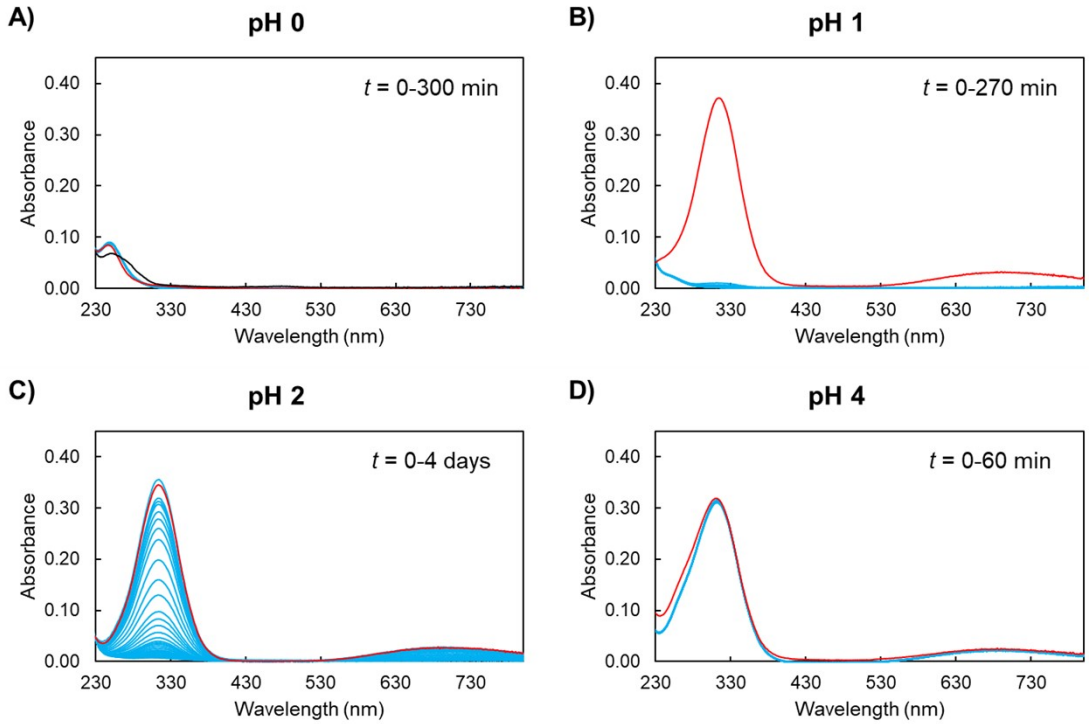

Figure S19. Examples of time-dependent UV-Vis spectra of solutions containing Cu^{2+} and DO4N (C_{Cu} = C_{DO4N} = 10^{-4} M, T = 298 K) at (A) pH 0 by 1 M HCl, (B) pH 1 by 0.1 M HCl, (C) pH 2 by 0.01 M HCl, and (D) pH 4 by 0.01 M acetic acid/acetate buffer (light blue). Red spectra indicate that the solution was heated at 65°C overnight. (A) The spectrum of 10^{-4} M $CuCl_2$ in 1 M HCl is also shown for comparison (black). The trend of absorbance *vs* time is shown in **Figure S22**.

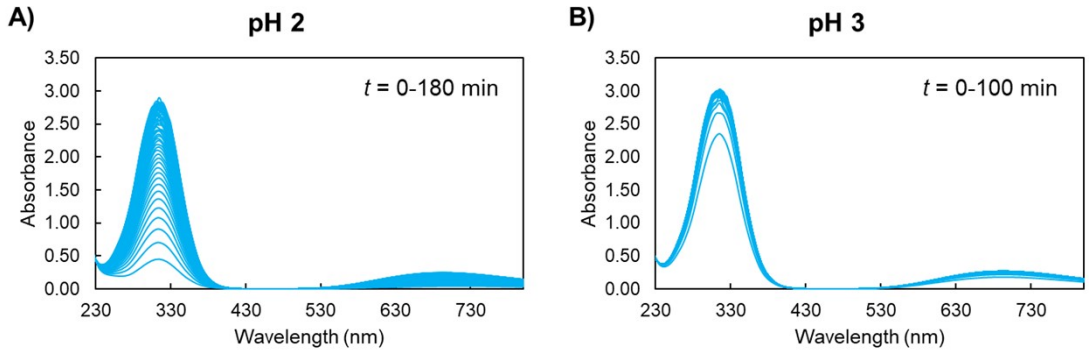

Figure S20. Time-dependent UV-Vis spectra of solutions containing Cu^{2+} and DO4N (C_{Cu} = C_{DO4N} = 10^{-3} M, T = 298 K) at (A) pH 2 by 0.01 M HCl and (B) pH 3 by 10^{-3} M HCl. The trend of absorbance *vs* time is shown in **Figure S23**.

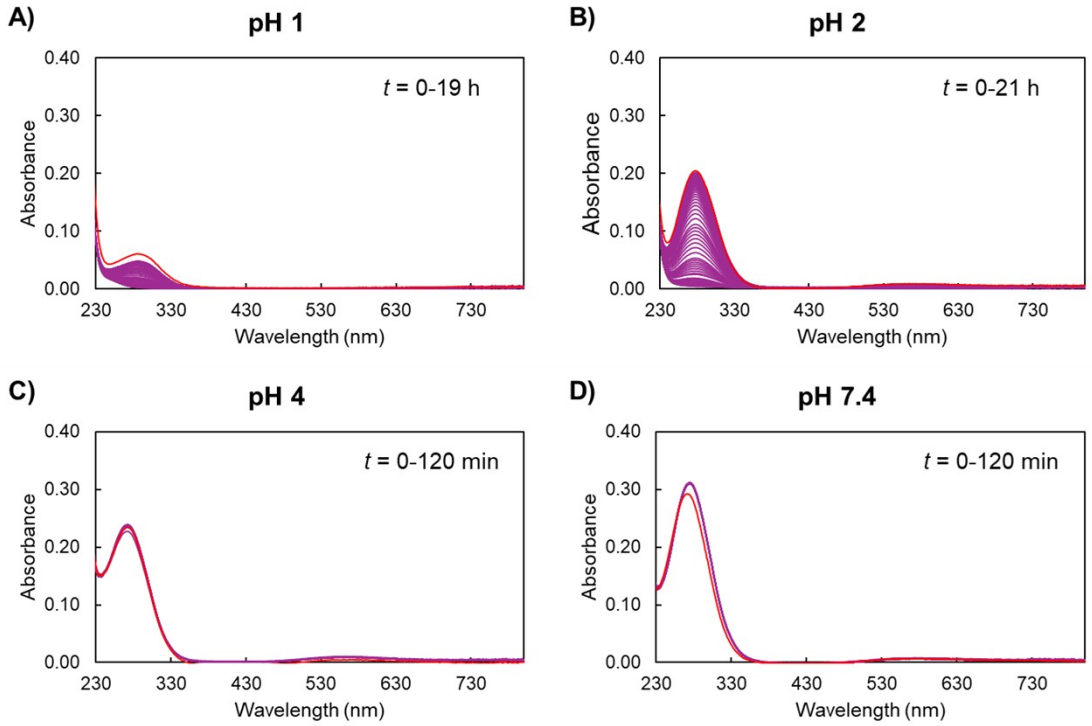

Figure S21. Time-dependent UV-Vis spectra of solutions containing Cu^{2+} and NO3N (C_{Cu} = C_{NO3N} = 10^{-4} M, T = 298 K) at (A) pH 1 by 0.1 M HCl, (B) pH 2 by 0.01 M HCl, (C) pH 4 by 0.01 M acetic acid/acetate buffer, and (D) pH 7.4 by 0.01 M HEPES buffer (purple). Red spectra indicate that the solution was heated at 65°C overnight. The trend of absorbance *vs* time is shown in **Figure S24**.

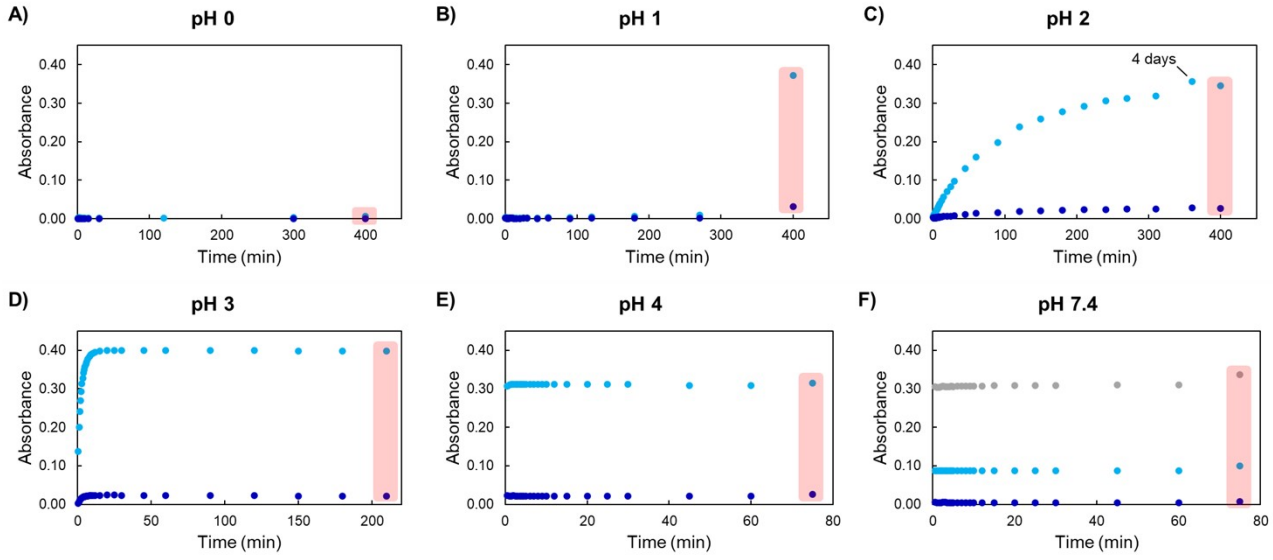

Figure S22. Kinetics of Cu^{2+}-DO4N complex formation by UV-Vis spectroscopy (C_{Cu} = C_{DO4N} = 10^{-4} M, T = 298 K) at (A) pH 0 by 1 M HCl, (B) pH 1 by 0.1 M HCl, (C) pH 2 by 0.01 M HCl, (D) pH 3 by 10^{-3} M HCl, (E) pH 4 by 0.01 M acetic acid/acetate buffer, and (F) pH 7.4 by 0.01 M HEPES buffer. Absorbance at either 270 nm (gray), 315 nm (light blue), or 690 nm (dark blue) is shown. Red shading indicates that the solution was heated at 65°C overnight (the point was inserted in the graph at an arbitrary abscissa). Examples of the corresponding UV-Vis spectra are shown in **Figure S19**.

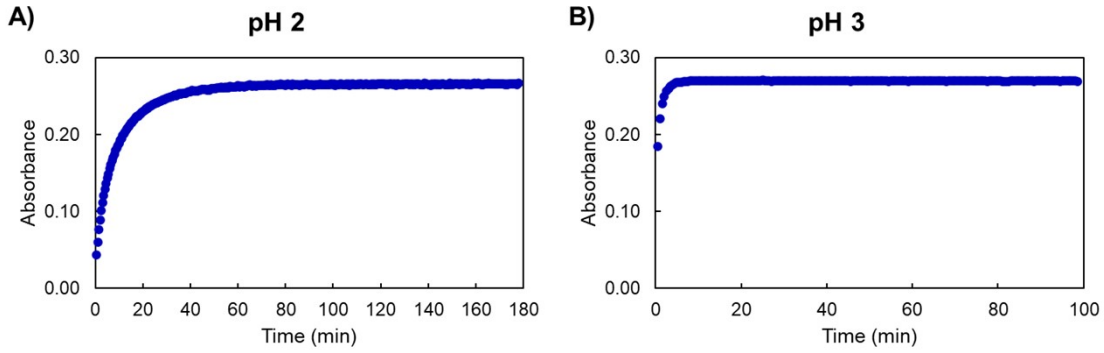

Figure S23. Kinetics of Cu^{2+}-DO4N complex formation by UV-Vis spectroscopy (C_{Cu} = C_{DO4N} = 10^{-3} M, T = 298 K) at (A) pH 2 by 0.01 M HCl and (B) pH 3 by 10^{-3} M HCl. Absorbance at 690 nm is shown. The corresponding UV-Vis spectra are shown in **Figure S20**.

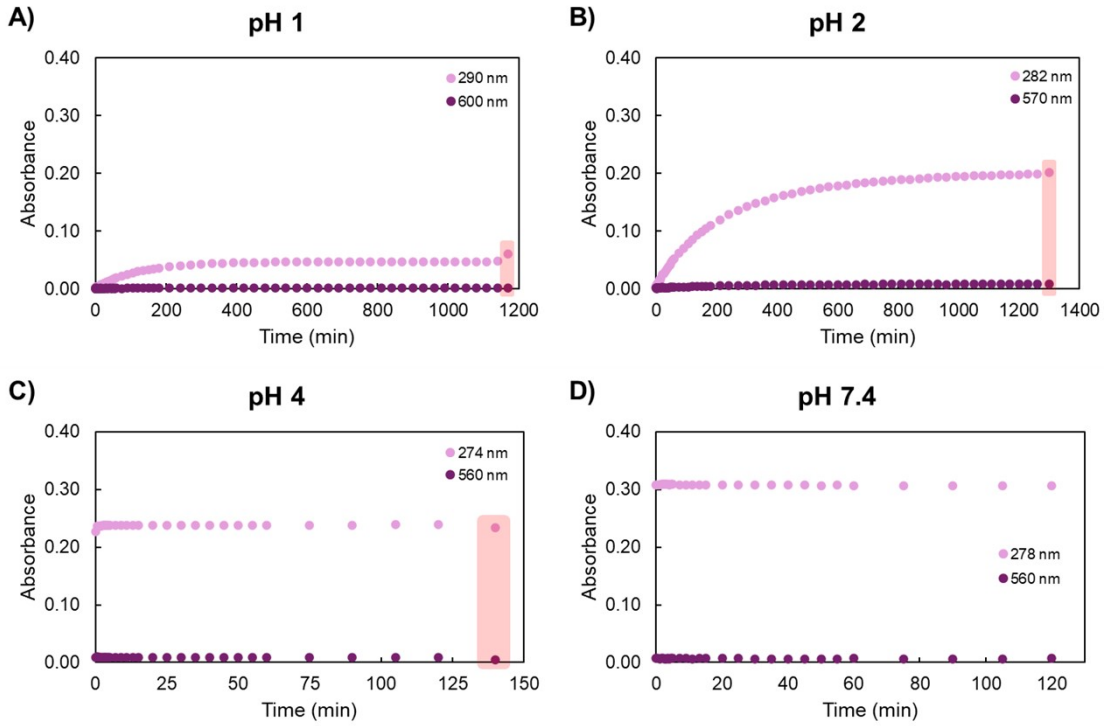

Figure S24. Kinetics of Cu^{2+}-NO3N complex formation by UV-Vis spectroscopy (C_{Cu} = C_{NO3N} = 10^{-4} M, T = 298 K) at (A) pH 1 by 0.1 M HCl, (B) pH 2 by 0.01 M HCl, (C) pH 4 by 0.01 M acetic acid/acetate buffer, and (D) pH 7.4 by 0.01 M HEPES buffer. Absorbance at either 274-290 nm (lilac) or 560-600 nm (purple) is shown. Red shading indicates that the solution was heated at 65°C overnight (the point was inserted in the graph at an arbitrary abscissa). The corresponding UV-Vis spectra are shown in **Figure S21**.

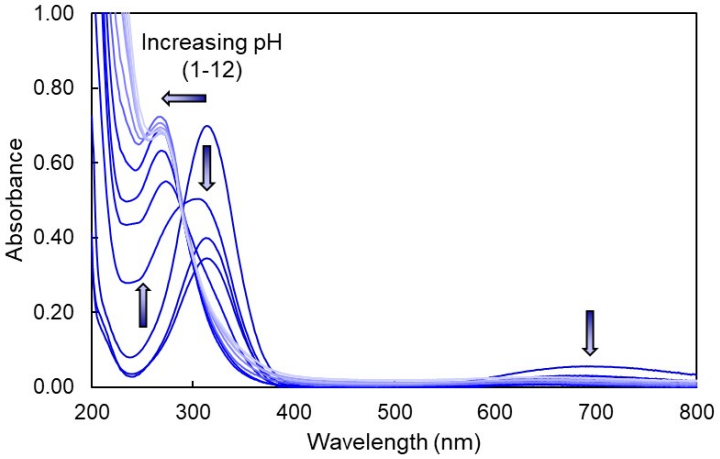

Figure S25. Representative spectra of a pH-dependent UV-Vis titration of Cu^{2+}-DO4N (C_{Cu} = C_{DO4N} = 10^{-4} M, T = 298 K, I = 0.15 M NaCl).

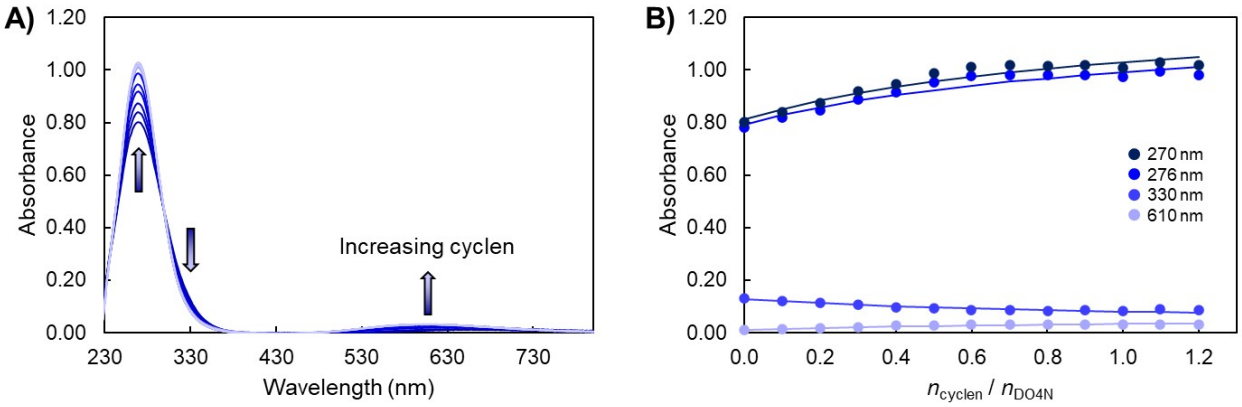

Figure S26. Competition between DO4N and cyclen for the complexation of Cu^{2+} by UV-Vis spectroscopy (C_{Cu} = C_{DO4N} = $2 \cdot 10^{-4}$ M, T = 298 K, pH 7.34 by 0.1 M HEPES buffer). (A) Spectra at different concentrations of cyclen (C_{cyclen} = 0-$2.4 \cdot 10^{-4}$ M). (B) Trend of absorbance at different wavelengths (270, 276, 330, 610 nm from top to bottom) *vs* cyclen/DO4N molar ratio (n_{cyclen} / n_{DO4N}) with fitting curves. See **Figure S31** for the individual Cu^{2+}-DO4N and Cu^{2+}-cyclen spectra.

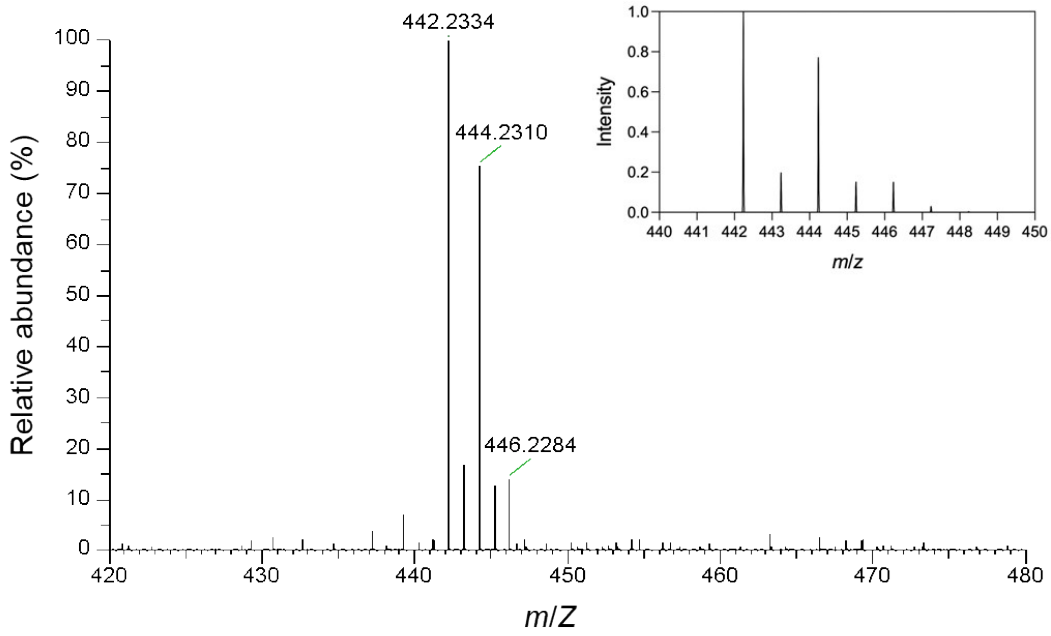

Figure S27. High-resolution electrospray ionization mass spectrum of Cu^{2+}-DO4N. The insert shows the simulated mass spectrum for $[CuCl(DO4N)]^+$, *i.e.* $[C_{16}H_{40}ClCuN_8]^+$: *m*/*Z* = 442.24 (100.0%), 444.23 (76.6%), 443.24 (17.8%), 446.23 (14.7%), 445.24 (13.6%), 447.23 (2.9%).

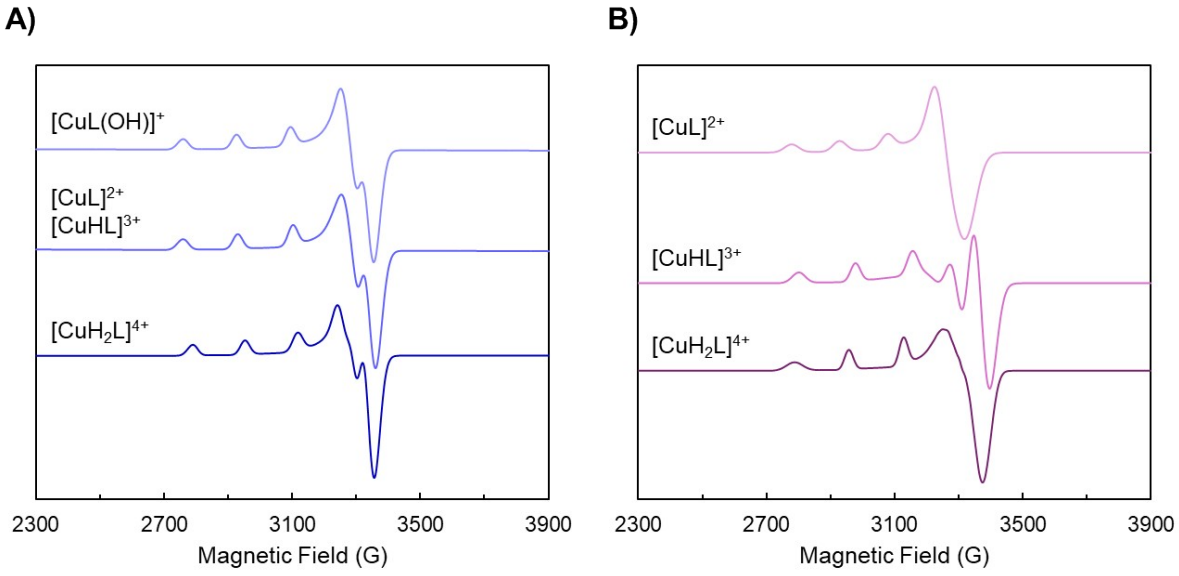

Figure S28. Frozen-solution EPR spectra of the single species composing (A) Cu^{2+}-DO4N and (B) Cu^{2+}-NO3N as computed during the fitting process (80% H_2O + 20% CH_3OH, 9.54 GHz, T = 77 K, I = 0.15 M NaCl, C_L = $2.2 \cdot 10^{-3}$ M, C_{Cu} = $2.0 \cdot 10^{-3}$ M).

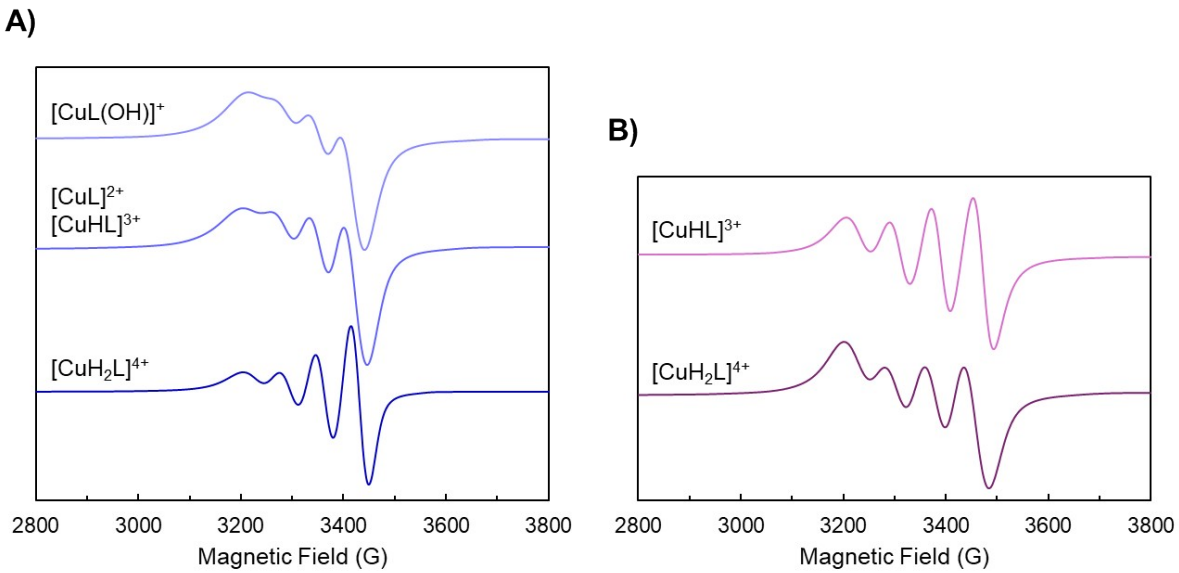

Figure S29. Room-temperature EPR spectra of the single species composing (A) Cu^{2+}-DO4N and (B) Cu^{2+}-NO3N as computed during the fitting process (H_2O, 9.54 GHz, T = 298 K, I = 0.15 M NaCl, C_L = $2.2 \cdot 10^{-3}$ M, C_{Cu} = $2.0 \cdot 10^{-3}$ M).

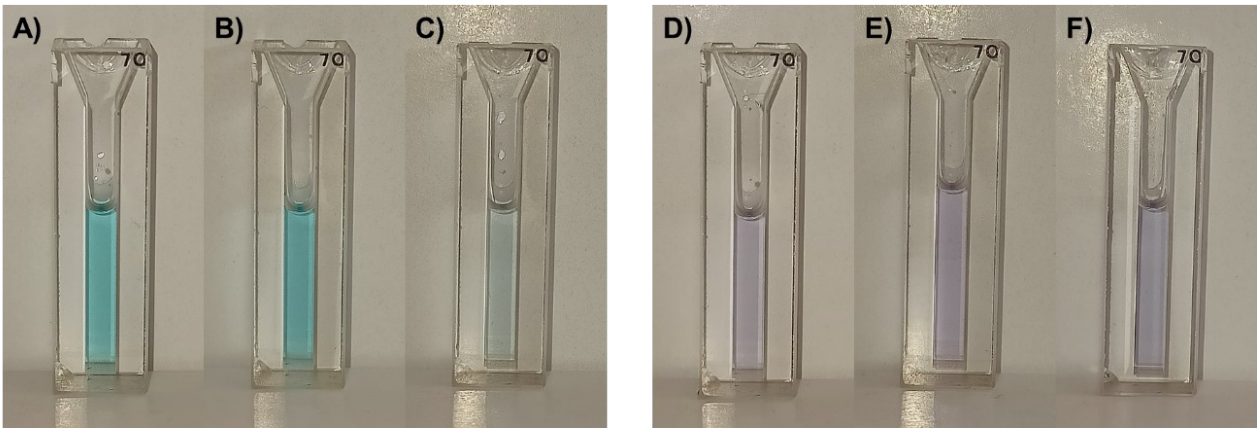

Figure S30. Color of solutions containing either Cu^{2+}-DO4N (A, B, C) or Cu^{2+}-NO3N (D, E, F) at (A, D) pH 2 by 0.01 M HCl, (B, E) pH 4 by 1 M acetic acid/acetate buffer, and (C, F) pH 7 by 1 M HEPES buffer (C_{Cu} = C_L = $7 \cdot 10^{-4}$ M, T = 298 K).

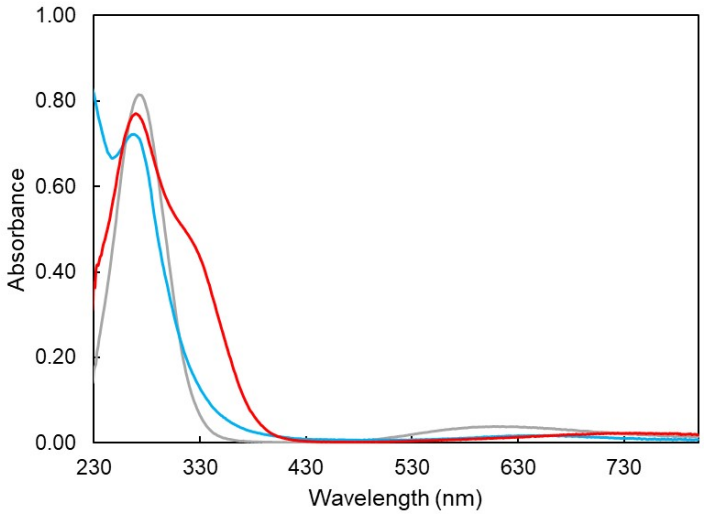

Figure S31. Comparison of the UV-Vis spectrum of Cu^{2+}-cyclen (gray), Cu^{2+}-DO4N (blue), and Cu^{2+}-DOTA (red) at pH 7.4 by 0.1 M HEPES buffer ($C_{Cu} = C_L = 2 \cdot 10^{-4}$ M, $T = 298$ K).

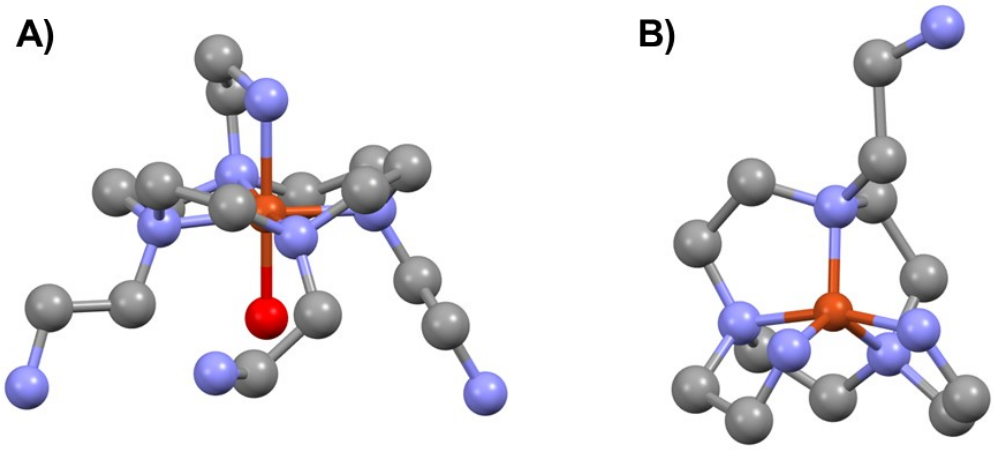

Figure S32. Proposed structure of (A) Cu^{2+}-DO4N complexes and (B) $[Cu(HNO3N)]^{3+}$ in aqueous solution based on EPR and UV-Vis spectroscopy, highlighting (A) an elongated octahedral $[4N]N_{ax}O_{ax}$ and (B) a distorted square pyramidal $[4N]N_{ax}$ coordination geometries. These structures were obtained by basic geometry optimization and are shown to better visualize the coordination modes. Hydrogen atoms are hidden for clarity. See the main text for a detailed discussion.

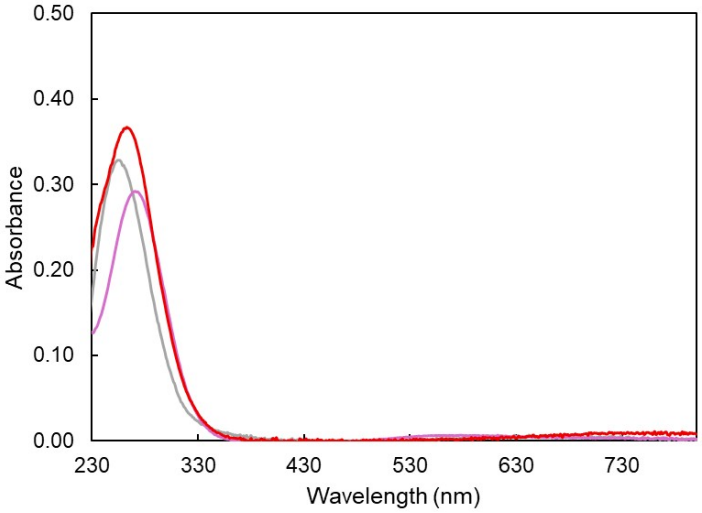

Figure S33. Comparison of the UV-Vis spectrum of Cu^{2+}-TACN (gray), Cu^{2+}-NO3N (lilac), and Cu^{2+}-NOTA (red) at pH 7.4 by 0.1 M HEPES buffer (C_{Cu} = C_L = 10^{-4} M, T = 298 K).

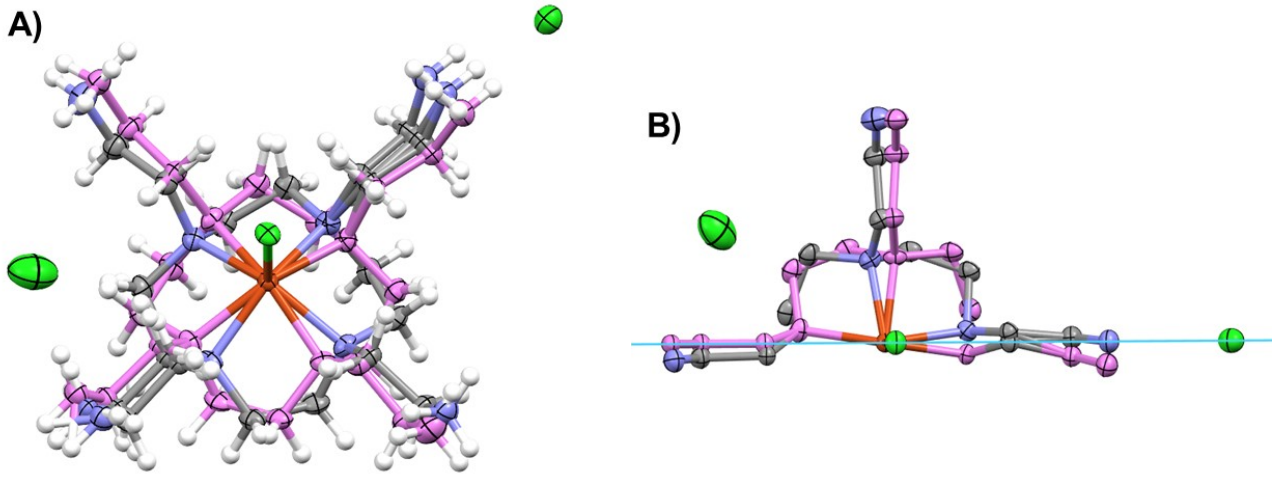

Figure S34. (A) ORTEP representation of the complex in the crystal $[Cu(H_2DO4N)Cl]Cl_3$ + solvent. Displacement parameters are drawn at 50% probability level. Both disordered conformations of the complex (chemical occupancy ratio 0.50/0.50) are shown. Molecule 1 is colored by element and molecule 2 is depicted in violet. (B) Asymmetrical unit of crystal $[Cu(H_2DO4N)Cl]Cl_3$ showing the mirror plane with a light blue line, splitting two side chains into two positions with a 0.25/0.25 occupancy.

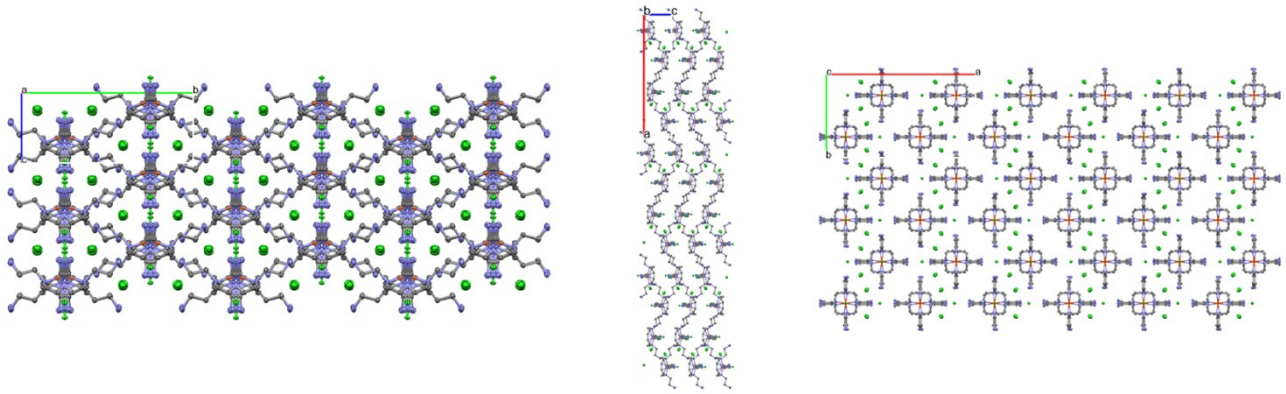

Figure S35. Packing arrangements of disordered molecule 1 in the crystal of $[Cu(H_2DO4N)Cl]Cl_3$ viewed from the crystallographic directions “a”, “b” and “c”.

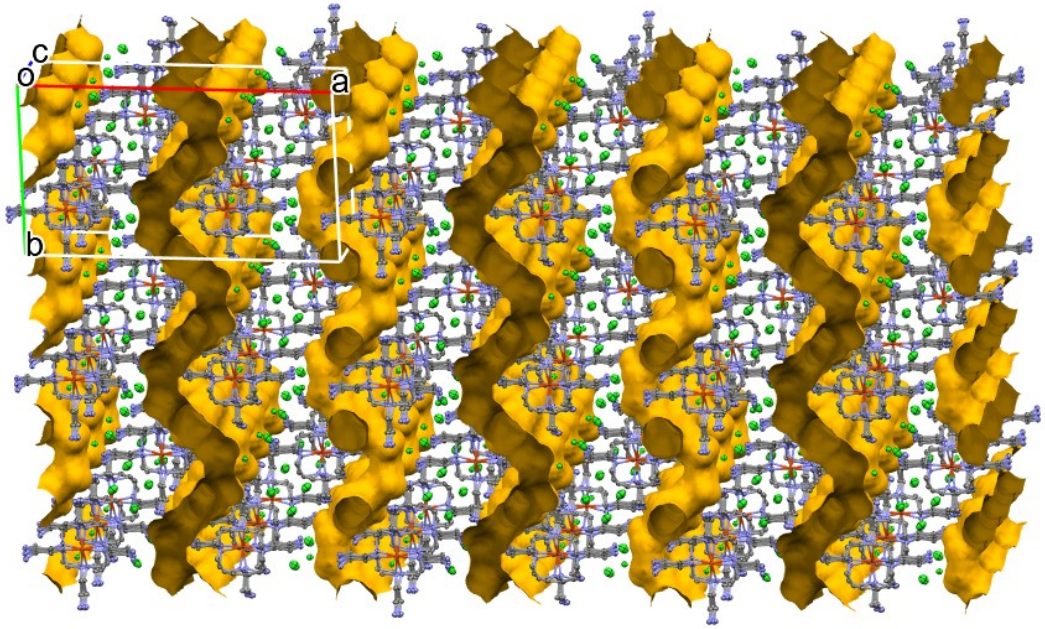

Figure S36. Packing arrangements in the crystal of $[Cu(H_2DO4N)Cl]Cl_3$ showing the channels occupied by the disordered solvent molecules. The void volume is 606 $Å^3$ (18.0% of the unit cell).

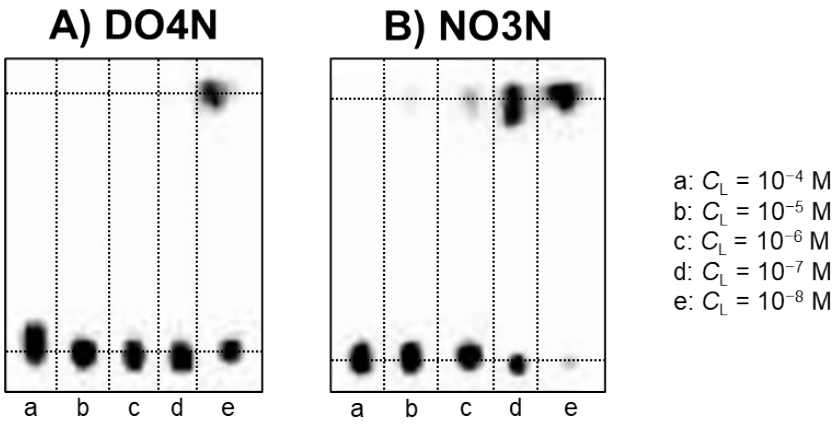

Figure S37. Representative radio-TLC for concentration-dependent (C_L = 10^{-4}-10^{-8} M) radiolabeling of (A) DO4N and (B) NO3N with [^{64}Cu]Cu^{2+} at pH 7 and T = 90°C (t = 10 min; 2-3 MBq ^{64}Cu, C_{Cu} = 2-3·10^{-9} M).

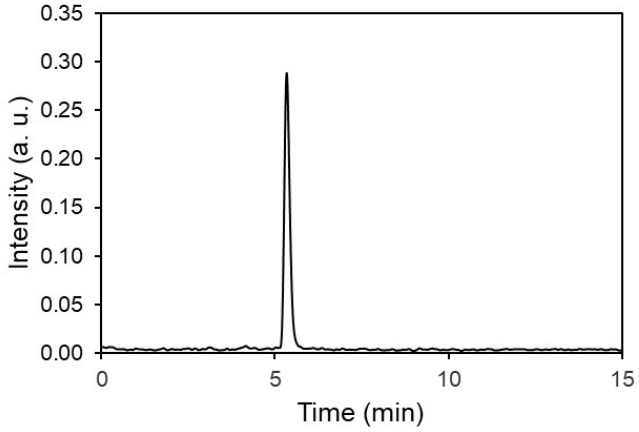

Figure S38. Representative radio-HPLC chromatogram of [^{64}Cu]Cu-DO4N.

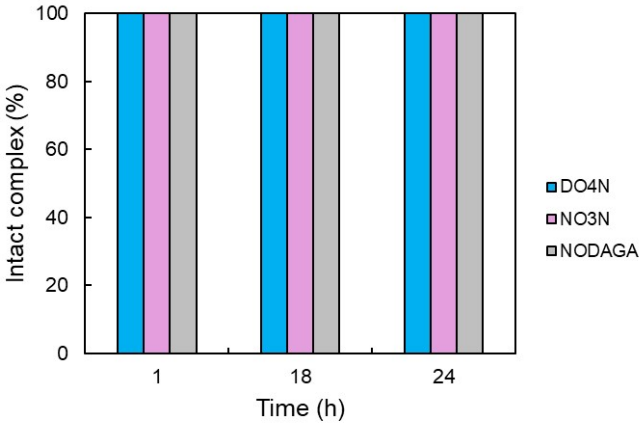

Figure S39. Time-dependent (1-24 h) stability of [^{64}Cu]Cu^{2+} complexes with DO4N, NO3N, and NODAGA in human serum (1/1 V/V complex-to-medium mixture, T = 37°C).

Supplementary Tables

Table S1. Electronic spectroscopy parameters of Cu^{2+} complexes with cyclen- or TACN-based chelators.

	λ_{max} (nm)	ε_{max} ($L \cdot mol^{-1} \cdot cm^{-1}$)	$\lambda_{d\text{-}d}$ (nm)	$\varepsilon_{d\text{-}d}$ ($L \cdot mol^{-1} \cdot cm^{-1}$)
Cyclen-based chelators				
$[Cu(H_2DO4N)]^{4+}$, $[Cu(HDO4N)]^{3+}$	315	$3.2\text{-}3.4 \cdot 10^3$	693	$3.6\text{-}3.7 \cdot 10^2$
$[Cu(DO4N)]^{2+}$	271	$3.4 \cdot 10^3$	654	70
$[Cu(cyclen)]^{2+}$	277	$4.0 \cdot 10^3$	596-610	$1.2\text{-}1.9 \cdot 10^2$
$[Cu(DOTA)]^{2-}$	272	$3.8 \cdot 10^3$	742	$1.2 \cdot 10^2$
[Cu(DO2A2S)]	272	$5.0 \cdot 10^3$	715	$1.6 \cdot 10^2$
TACN-based chelators				
$[Cu(H_2NO3N)]^{4+}$, $[Cu(HNO3N)]^{3+}$	276-280	$2.0\text{-}3.0 \cdot 10^3$	567-573	$1.0\text{-}1.3 \cdot 10^2$
$[Cu(TACN)]^{2+}$	256	$3.3 \cdot 10^3$	625	82
[Cu(HNOTA)] (ref. [5,6])	n.a.	n.a.	660	$1.1 \cdot 10^2$
$[Cu(NOTA)]^{-}$	265	$3.4\text{-}3.7 \cdot 10^3$	750 [a]	84-99 [a]

[a] These values are in agreement with those reported in ref. [5,6]. n.a. Data not available.

Table S2. Crystal data and structure refinement for $[Cu(H_2DO4N)Cl]Cl_3$ + solvent.

CCDC number	2468463
Identification code	CuDO4N
Empirical formula	$C_{16}H_{42}Cl_4CuN_8$ + solvent
Formula weight	551.91
Temperature (K)	100 (2)
Crystal system	Orthorhombic
Space group (number)	*Pnma* (62)
a (Å)	29.8294 (11)
b (Å)	16.6394 (7)
c (Å)	6.7840 (3)
α (°)	90
β (°)	90
γ (°)	90
Volume (Å^3)	3367.2 (2)
Z/*Z*'	4/0.5
ρ_{calc} (g/cm^3)	1.089
μ (mm^{-1})	0.981
F(000)	1164
Crystal size (mm^3)	0.067 x 0.105 x 0.118
Crystal color	Light blue
Crystal shape	Block
Radiation	MoK_α (λ = 0.71073 Å)
2Θ range for data collection (°)	4.896 to 56.57 (0.75 Å)
Index ranges	−31 ≤ h ≤ 39, −22 ≤ k ≤ 22, −9 ≤ l ≤ 9
Reflections collected	59943
Independent reflections	4303 [R_{int} = 0.0512, R_{sigma} = 0.0220]
Completeness to θ = 25.242°	99.9
Data/restraints/parameters	4303/431/343
Goodness-of-fit on F^2	1.045
Final *R* indexes [$I \geq 2\sigma$ (I)]	R_1 = 0.0527, wR_2 = 0.1489
Final *R* indexes [all data]	R_1 = 0.0616, wR_2 = 0.1569
Largest diff. peak/hole (e Å^{-3})	1.52/−1.12

Supplementary References

1. M. Tosato, M. Dalla Tiezza, N.V. May, A.A. Isse, S. Nardella, L. Orian, *et al.* Copper Coordination Chemistry of Sulfur Pendant Cyclen Derivatives: An Attempt to Hinder the Reductive-Induced Demetalation in $^{64/67}$Cu Radiopharmaceuticals, *Inorg. Chem.*, 2021, **60**, 11530–47.
2. M. Tosato, M. Pelosato, S. Franchi, A.A. Isse, N.V. May, G. Zanoni, *et al.* When Ring Makes the Difference: Coordination Properties of Cu^{2+}/Cu^{+} Complexes with Sulfur-Pendant Polyazamacrocycles for Radiopharmaceutical Applications, *New J. Chem*., 2022, **46**, 10012–25.
3. M. Tosato, S. Franchi, A.A. Isse, A. Del Vecchio, G. Zanoni, A. Alker, *et al.* Is Smaller Better? Cu^{2+}/Cu^{+} Coordination Chemistry and Copper-64 Radiochemical Investigation of a 1,4,7-Triazacyclononane-Based Sulfur-Rich Chelator, *Inorg. Chem.*, 2023, **62**, 20621–33.
4. L. Tei, A. Bencini, A.J. Blake, V. Lippolis, A. Perra, B. Valtancoli, *et al.* Coordination Chemistry of Amino Pendant Arm Derivatives of 1,4,7-Triazacyclononane, *Dalton Trans.,* 2004, **13**, 1934–44.
5. A. Bevilacqua, R.I. Gelb, W.B. Hebard, L.J. Zompa, Equilibrium and Thermodynamic Study of the Aqueous Complexation of 1,4,7-Triazacyclononane-*N*,*N*',*N*''-triacetic Acid with Protons, Alkaline-Earth-Metal Cations, and Copper(II), *Inorg. Chem.,* 1987, **26**, 2699–706.
6. C.F.G.C. Geraldes, M.P.M. Marques, B. De Castro, E. Pereira, Study of Copper(II) Polyazamacrocyclic Complexes by Electronic Absorption Spectrophotometry and EPR Spectroscopy, *Eur. J. Inorg. Chem.,* 2000, **3**, 559–65.